Full length article

Morphological stability of rod-shaped continuous phases

Fei Wang[a,*], Oleg Tschukin[a], Thomas Leisner[c,d], Haodong Zhang[a], Britta Nestler[a,b], Michael Selzer[a,b], Gabriel Cadilha Marques[e,f], Jasmin Aghassi-Hagmann[e,g]

[a] *Institute of Applied Materials-Computational Materials Science, Karlsruhe Institute of Technology (KIT), Strasse am Forum 7, Karlsruhe 76131, Germany*
[b] *Institute of Digital Materials Science, Karlsruhe University of Applied Sciences, Moltkestraße 30, Karlsruhe 76133, Germany*
[c] *Institute of Environmental Physics, University of Heidelberg, Im Neuenheimer Feld 229, Heidelberg 69120, Germany*
[d] *Institute of Meteorology and Climate Research, Karlsruhe Institute of Technology (KIT), Hermann-von-Helmholtz-Platz 1, Eggenstein-Leopoldshafen 76344, Germany*
[e] *Institute of Nanotechnology, Karlsruhe Institute of Technology (KIT), Hermann-von-Helmholtz-Platz 1, Eggenstein-Leopoldshafen 76344, Germany*
[f] *Department of Computer Science, Karlsruhe Institute of Technology (KIT), Haid-und-Neu-Str. 7, Karlsruhe 76131, Germany*
[g] *Department of Electrical Engineering and Information Technology, Offenburg University of Applied Sciences, Offenburg 77652, Germany*

A B S T R A C T

Morphological transition of a rod shaped phase into a string of spherical particles is commonly observed in the microstructures of alloys during solidification (Ratke and Mueller, 2006). This transition phenomenon can be explained by the classic Plateau Rayleigh theory which was derived for fluid jets based on the surface area minimization principle. The quintessential work of Plateau Rayleigh considers tiny perturbations (amplitude much less than the radius) to the continuous phase and for large amplitude perturbations, the breakup condition for the rod shaped phase is still a knotty issue. Here, we present a concise thermodynamic model based on the surface area minimization principle as well as a non linear stability analysis to generalize Plateau Rayleigh's criterion for finite amplitude perturbations. Our results demonstrate a breakup transition from a continuous phase via dispersed particles towards a uniform radius cylinder, which has not been found previously, but is observed in our phase field simulations. This new observation is attributed to a geometric constraint, which was overlooked in former studies. We anticipate that our results can provide further insights on microstructures with spherical particles and cylinder shaped phases.

Keywords:
Plateau-Rayleigh instability
Phase-field
Surface area minimization
Gradient descent method

1. Introduction

The transition of a rod shaped continuous phase into a chain of spherical particles is a widely observed phenomenon in materials sci ence. As shown in Fig. 1(a), during the solidification of the Al Bi alloys [1], the continuous L_2 phase (dark) transforms into a stream of pearls. This kind of morphological transition is also observed in the solidified microstructures of Al In alloys [2] as well as for annealed Ag nano wires [3], as illustrated in Fig. 1(b) and Fig. 1(c), respectively. Another daily observation for this transition is depicted in Fig. 1(d) (f), where a water jet trickles down under a water tap and eventually breaks apart into a chain of droplets. This morphological transition phenom enon has drawn broad interests both in fundamental researches [4 15] and practical applications [16 20].

The breakup condition is firstly tackled by Joseph Plateau [21] and Lord Rayleigh for fluid jets [22]. They consider a cosinusoidal pertur bation to an infinitely long continuous phase, as depicted in Fig. 1(g). The surface of the perturbed phase at the beginning is represented by

$$r \quad R_0^o + a_1^o \cos kz. \tag{1}$$

Here, R_0^o is a reference radius (see Fig. 1(g)), a_1^o and k are the ampli tude and wavenumber of the perturbation, respectively, and z is the coordinate along the longitudinal dimension of the rod shaped phase. Assuming tiny perturbations, i.e. $a_1^o/R_0^o \ll 1,$ The difference between the surface area after perturbation S and the one for a uni form radius cylinder S_u is expressed as [23].

$$S \quad S_u \quad \frac{1}{4}\frac{\pi(a_1^o)^2}{R_u\lambda}\left[(2\pi R_u)^2 \quad \lambda^2\right]. \tag{2}$$

It is noteworthy that R_u is the radius of a cylinder which has the same volume as the perturbed phase and S_u is a product of the perimeter $2\pi R_u$ with the wavelength $\lambda \quad 2\pi/k,$ namely, $S_u \quad 2\pi R_u\lambda$. Based on Eq. (2), it is claimed that in order to reduce the surface area, the per turbation increases its amplitude when $\lambda > 2\pi R_u$, leading to a mor phological instability. Otherwise, the perturbation dissipates with time, engendering a uniform radius cylinder. Hence, the critical wavelength demarcating the morphological stable and unstable regions is

* Corresponding author.
E-mail address: fei.wang@kit.edu (F. Wang).

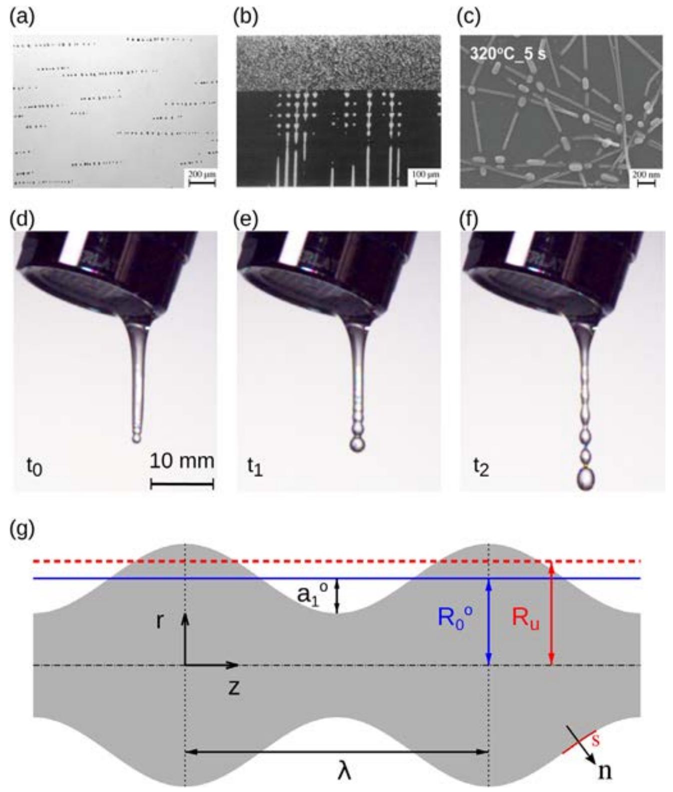

Fig. 1. Morphological transition of a rod-shaped phase into spherical particles. (a) Al-Bi alloys [1]. Reuse with permission, ©2006, Elsevier. (b) Al-In alloys [2]. Reuse with permission, ©1991, Elsevier. (c) Ag nanowires [3]. Reuse with permission, ©2006, IOP. (d)-(f) Formation of water droplets under a water-tap. t_0 = 0 ms, t_1 = 8.0 ms, t_2 = 25.3 ms. (g) 2D projection of a perturbed phase $r \quad R_0^o + a_1^o\cos(2\pi z/\lambda)$, where a_1^o and λ are the amplitude and the wavelength of the initial harmonic perturbation, respectively. The volume of the phase is $\int_0^\lambda \pi r^2 dz \quad \pi\left[(R_0^o)^2 + \frac{1}{2}(a_1^o)^2\right]\lambda$ and we define $R_u^2 \quad (R_0^o)^2 + \frac{1}{2}(a_1^o)^2$ as the mean radius.

$$\lambda_{\text{crit}}^R \quad 2\pi R_u. \tag{3}$$

This result is known as the Plateau Rayleigh's criterion [21,23].

Plateau Rayleigh's work only considers tiny perturbations, which are unlikely to be always the cases in reality, and sometimes, is incon sistent with experimental observations. For instance, it has been measured by Marinis that some instability wavelengths of MnSb fibres in the MnSb Sb eutectic are in the range of $(0.79 \quad 0.95)2\pi R_u$ [24], which is less than Plateau Rayleigh's critical wavelength. In order to provide potential interpretations on those observed incon sistencies, Carter and Glaeser [25] extend Plateau Rayleigh's work by considering finite amplitude perturbations, e.g. $0 < a_1^o/R_0^o < 1$. As derived in Ref. [25], the surface area of the perturbed phase is given by the following integral as

$$S \quad \int_0^\lambda 2\pi r\sqrt{1 + (\partial_z r)^2}dz. \tag{4}$$

For tiny perturbations ($a_1^o/R_0^o \ll 1$), the integration Eq. (4) can be approximated by Eq. (2). Such an approximation is actually the quin tessential derivation of Plateau and Rayleigh [21,23]. However, for finite amplitude perturbations ($0 < a_1^o/R_0^o < 1$), the integration Eq. (4) does not have a closed form. In this case, the surface area at the per turbed state can only be obtained via a numerical integration for Eq. (4), as elucidated by Carter and Glaeser [25]. Calculating the sur face area landscape S as a function of the amplitude a_1^o and using the surface area minimization principle to judge if the amplitude increases or decreases with time, a stability criterion $\lambda_{\text{crit}}/2\pi R_u$ versus a_1^o/R_0^o is obtained by Carter and Glaeser. This criterion does not have a closed form. Following the same method of Carter and Glaeser, Ma et al. [26] found that the critical wavelength linearly depends on the square of a_1^o/R_0^o as

$$\lambda_{\text{crit}}^{CG} \quad 2\pi R_0^o[1 \quad 0.34(a_1^o/R_0^o)^2], \tag{5}$$

which is termed as Carter Glaeser & Ma criterion in the following. It is obvious to see that this result is consistent with Plateau Rayleigh's crite rion when $a_1^o/R_0^o \ll 1$. This critical wavelength is less than the one of Pla teau Rayleigh, when the ratio a_1^o/R_0^o is non negligible in comparison to unity, this critical wavelength is less than the one of Plateau Rayleigh.

In these progressive works, the calculation for the surface area is based on an assumption that the surface of the perturbed phase is perpetually described by a harmonic function at any time t, namely,

$$r(t,z) \quad R_0(t) + a_1(t)\cos kz. \tag{6}$$

This assumption is quite idealized. In fact, with time the initially cosi nusoidal perturbation is very likely to get disordered gradually, in lieu of remaining harmonic [27,28]. That is, higher order terms a_i, $i \geq 2$ may occur during the time evolution, although we only have the a_1 term at the very beginning $t \quad 0$. In the current work, we will present a generalized stability criterion by considering those higher order terms overlooked in previous investigations. Our stability crite rion is further corroborated by phase field simulations as well as by a non linear stability analysis.

2. Phase-field model

The underlying mechanism for the surface area minimization is the non uniform capillary force/mean curvature along the surface of the perturbed phase. Thus, the detachment of a rod shaped phase is a curvature driven problem, which can be modeled by the phase field model [29,30]. The advantage of this model is that an explicit tracking of the interface is avoided.

In the phase field model, a time and space dependent phase order parameter $\phi(\mathbf{x}, t)$ is introduced to characterize the phase state. This order parameter can be interpreted as the local volume fraction of the phase. For instance, $\phi \quad 1$ in the bulk of the continuous phase, $\phi \quad 0$ in the bulk of the surrounding phase, and $0 < \phi < 1$ across the interface from the continuous phase to the surrounding. The time evolution of the order parameter is such as to reduce the free energy functional $\mathcal{G}$ of the system, following the variational approach as

$$\tau\epsilon\partial_t\phi \quad \delta\mathcal{G}/\delta\phi, \tag{7}$$

where τ is a relaxation parameter and ϵ is a length parameter related to the thickness of the phase surrounding interface. The symbol δ denotes the operator for the functional derivative. The evolution equation Eq. (7) is known as the Allen Cahn model [31]. As shown in Ref. [32], the free energy functional of the system is expressed as

$$\mathcal{G} \quad \int_V\left[\sigma\epsilon(\nabla\phi)^2 + \frac{16}{\pi^2}\sigma\epsilon\phi(1 \quad \phi) + g(\phi)\right]dV.$$

Here, σ is the surface energy of the phase surrounding interface and $g(\phi)$ is a free energy density to ensure that the volume of the continu ous phase is conserved, namely, $\int_V\partial_t\phi \quad 0$ (see Ref. [32,33] for more details).

The system evolution equation Eq. (7) is discretized by the central finite difference method and the explicit Euler scheme. The space, time and energy are non dimensionalized by $x^* \quad 1\times10^{-6}$ m, $t^* \quad 1\times10^{-9}$ s and $E^* \quad 1\times10^{-11}$ J, respectively. The dimensionless simula tion parameters are $\sigma \quad 1$, $\epsilon \quad 6$, $\tau \quad 1$, $\Delta x \quad \Delta y \quad \Delta z \quad 1$, and $\Delta t \quad 0.01$, where Δx and Δt are the discretized space and time steps, respectively. A parallelization of the numerical algorithm is achieved with Message Passing Interface (MPI) techniques. The initial condi tion for the simulation is a perturbed phase whose surface is described by $r \quad R_0^o + a_1^o\cos kz$ at the center of the simulation domain with a size of 100 × 100 × λ. Periodic boundary conditions are applied in the longitudinal dimension (z), while Neumann boundary conditions are utilized in the other two dimensions (x and y).

Fig. 2 shows the morphological transition with three different initial amplitudes: a_1^o/R_0^o 0.10, 0.70 and 0.92. For each amplitude, we focus on three normalized wavelengths: one above Plateau Rayleigh's critical wavelength $\lambda/(2\pi R_u)$ 1.05, two below Plateau Rayleigh's critical wavelength $\lambda/(2\pi R_u)$ 0.80 and 0.37. For the small amplitude perturbation a_1^o/R_0^o 0.10, the continuous phase breaks up when $\lambda/(2\pi R_u)$ 1.05 (Fig. 2(a), i) and evolves into a uniform radius cylinder when $\lambda/(2\pi R_u)$ 0.80 and 0.37 (Fig. 2(a), ii and iii). This observation is consistent with Plateau Rayleigh's critical wavelength Eq. (3). For the intermediate amplitude perturbation a_1^o/R_0^o 0.70, the continuous phase transforms into spherical particles when $\lambda/(2\pi R_u)$ 0.80, which implies an inconsistency with Eq. (3) as well as with Eq. (5). For the large amplitude perturbation a_1^o/R_0^o 0.92, the inconsistency also appears for $\lambda/(2\pi R_u)$ 0.8. Besides, we observe an unusual morphological transition for $\lambda/(2\pi R_u)$ 0.37: continuous phase → dispersed particles → uniform radius cylinder. It is noteworthy that these small, medium and large amplitude perturbations may be observed in the microstructures of off eutectic compositions [34,35] or monotectic alloys [36], when the production phase exhibits an oscillatory behavior. In the following, we will attempt to address these inconsistencies by considering the effect of the perturbation amplitude on the breakup criterion.

3. Surface area minimization and surface area landscape method

As aforementioned and shown in Fig. 2, although a single cosine function is considered at the very beginning (Eq. (1)), the surface of the perturbed phase does not necessarily remain harmonic with time. Hence, we write the surface of the perturbed phase at any time t before the breakup by a Fourier series as

$$r(t,z) \quad R_0(t) + \sum_{n\ \ 1}^{K} a_n(t)\cos nkz, \tag{8}$$

where K is the dimension of the Fourier transformation, i.e. K 100 in the present work, and a_n is the n th amplitude or Fourier coefficient. Because of the symmetrical configuration, the contribution of sinusoidal terms to the Fourier series has been dropped. The reduction in the surface area is achieved by the time evolution of $R_0(t)$ and $a_n(t)$ with the initial conditions:

$$R_0(0) \quad R_0^o, \quad a_1(0) \quad a_1^o, \quad a_n(0) \quad 0, \ n \geq 2. \tag{9}$$

The surface of the perturbed phase at time t is expressed by the following surface integral S $\int_S 2\pi r ds$, where s is the arc length along the longitudinal dimension (see Fig. 1(g)). By using the relation ds^2 $dr^2 + dz^2$, the surface integral in one period is further rewritten as

$$S\Big(a_1(t), a_2(t), \cdots\Big) \quad 2\pi \int_0^{\lambda} \left[\mathrm{R_0(t)} + \sum_{\mathrm{n\ \ 1}}^{\mathrm{K}} \mathrm{a_n(t)\cos nkz}\right] \sqrt{1 + \Big(\textstyle\sum_{\mathrm{n\ \ 1}}^{\mathrm{K}} \mathrm{nka_n(t)\sin nkz}\Big)^2}\,\mathrm{dz}. \tag{10}$$

This surface integral has to be subjected to the condition that the volume of the perturbed phase is conserved: $V(t)$ $\pi R_u^2 \lambda$, which is a product of the surface area with the wavelength. The volume integration reads $V(t)$ $\int_0^{\lambda} \pi r^2 dz$. Hence, the volume constraint yields the following condition

$$R_u^2 \quad R_0^2(t) + \frac{1}{2}\sum_{n\ \ 1}^{K} a_n^2(t). \tag{11}$$

Substituting Eq. (11) into Eq. (10), we obtain the final expression for the calculation of the surface area landscape

$$S\Big(a_1(t), a_2(t), \cdots\Big) \quad 2\pi \int_0^{\lambda} \left(\sqrt{\mathrm{R_u^2} \quad \frac{1}{2}\textstyle\sum_{\mathrm{n\ \ 1}}^{\mathrm{K}} \mathrm{a_n^2(t)}} + \sum_{\mathrm{n\ \ 1}}^{\mathrm{K}} \mathrm{a_n(t)\cos nkz}\right) \sqrt{1 + \Big(\textstyle\sum_{\mathrm{n\ \ 1}}^{\mathrm{K}} \mathrm{nka_n(t)\sin nkz}\Big)^2}\,\mathrm{dz}. \tag{12}$$

For a given wavelength λ, we visualize the surface area landscape $S(a_1, a_2)$ for all possible values of the two Fourier coefficients a_1 and a_2. Three typical surface area landscapes S as a function of a_1/R_0 and a_2/R_0 are illustrated in Fig. 3(a), (b), and (c) for short ($\lambda/(2\pi R_u)$ 0.37), long ($\lambda/(2\pi R_u)$ 1.05), and medium wavelengths ($\lambda/(2\pi R_u)$ 0.80), respectively. These parameters are consistent with the simulation setups shown in Fig. 2. The contour levels of the surface area are indicated by the numbers on the broken solid lines. For the short wavelength (Fig. 3(a)), the global minimum of the surface area is at a_1 0 and a_2 0, so that the end state of any perturbed phase is a uniform radius cylinder. Contrarily, for the long wavelength (Fig. 3(b)), the global minimum is nearby the maximal value of a_1. In this case, the first amplitude of any perturbations a_1 has to continuously increase with time to reduce the surface area and the final state is a chain of spherical particles.

Interestingly, for the intermediate wavelength (Fig. 3(c)), two local minima locate inside the hatched and the dotted regions, which correspond to a final state of a uniform radius cylinder and a line of spherical particles, respectively. These two regions are partitioned by the contour lines (magenta lines) of the saddle point of the surface area, where $\partial_{a_1} S$ 0 & $\partial_{a_2} S$ 0. The domain outside these two regions, which is presently called as barrier zone, highlights initial configurations whose surface area is greater than the ones in the hatched and dotted regions and can evolve either into a uniform radius cylinder or into droplets. As aforementioned, we consider the evolution of a perturbed phase with a cosinusoidal perturbation with a_2^o 0 at the beginning. This initial setup corresponds to the horizontal dot dashed line in Fig. 3(c) and overlaps the barrier zone between the two gray circles embracing a barrier interval. Here, the meaning of the barrier zone or interval is that once the state is inside the hatched or dotted region, the continuous phase cannot move into the other one, since the surface area outside the hatched and dotted regions is greater than that in these two regions. Hence, the area outside the hatched and dotted regions is termed as barrier zone or interval. The critical configuration for the breakup buries inside the barrier interval, which is also obtained for many other medium wavelengths less and greater than $\lambda/(2\pi R_u)$ 0.80. All of those barrier intervals versus wavelengths is represented by the shaded region in Fig. 4(a). Left below and right

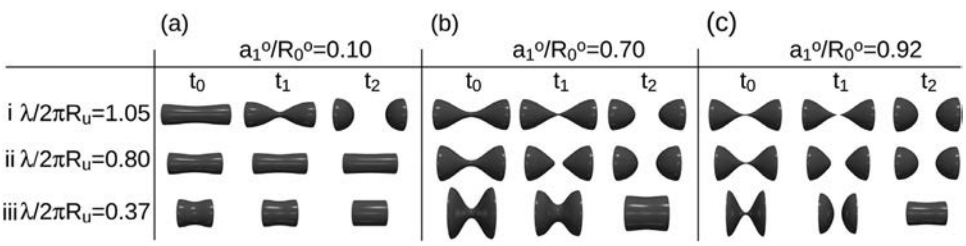

Fig. 2. Morphological evolution of rod-shaped phases with different amplitudes a_1^o/R_0^o and wavelengths $\lambda/(2\pi R_u)$ via phase-field simulations.

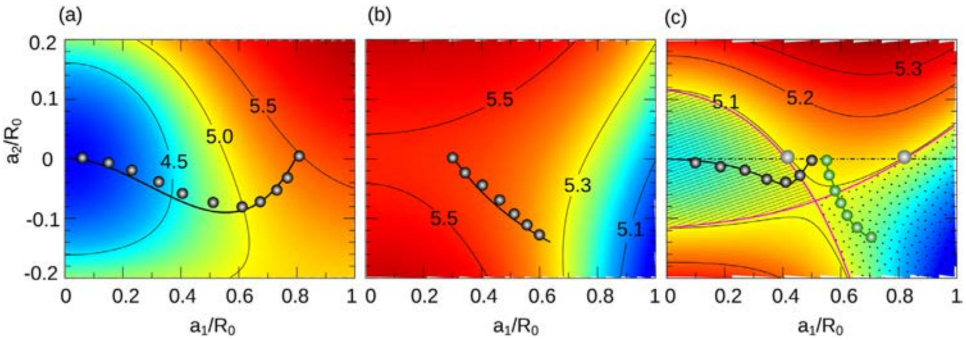

Fig. 3. Surface area landscape. (a), (b), (c), Surface area as a function of all the possible values of the first two Fourier coefficients (a_1/R_0 and a_2/R_0) with normalized wavelengths $\lambda/(2\pi R_u)$ 0.37, 1.05, 0.80, respectively. The black/green circles denote the evolution routes of a_1/R_0 and a_2/R_0 from the phase-field simulations. The black/green curves represent the evolution paths from the gradient descent method. The gray circles in (c) embrace a barrier interval along the horizontal dot-dashed line a_2/R_0 0. The hatched and dotted regions in (c) are partitioned by the isolines (magenta lines) of the saddle point of the surface area landscape. The contour values of the surface area are indicated by the numbers upon the isolines. Here, the surface area is obtained via the numerical integration Eq. (12) for a constant volume V 1 with different ratios of ξ : $\lambda/(2\pi R_u)$. In this calculation, the wavelength λ and radius R_u are expressed as λ $(4\pi V\xi^2)^{1/3}$ and R_u $\sqrt{V/(\pi\lambda)}$, respectively. With an increase or decrease in the volume, the contour values of the surface area have to be rescaled accordingly but the positions of the contour line do not change.

above this shaded region, the perturbed phase has a surface area landscape as in Fig. 3(a) and Fig. 3(b), respectively.

Next, we adopt the gradient descent method (GDM) to scrutinize the evolution path and the critical breakup configuration. The evolution direction of the Fourier coefficients follows the gradient of the surface area $(\partial_{a_n}S) \in \mathbb{R}^K$, namely,

$$\partial_t a_n \quad \Gamma \partial_{a_n} S, \tag{13}$$

where Γ is a kinetic coefficient. The time evolution is subjected to the initial condition Eq. (9) and the reference radius $R_0(t)$ is obtained according to the volume constraint Eq. (11). In Appendix A, we compare the time evolutions of the interface of the perturbed continuous phase from the gradient descent method and the phase field simulations. As can be seen from the comparison, the time evolution from these two approaches shows quite good agreement.

In Fig. 3(a) and Fig. 3(b), the black solid lines depict the kinetic routes along the steepest gradient for two initial setups a_1^o/R_0^o 0.80 and 0.30, respectively. In the former case, the first amplitude a_1 continuously decreases with time, resulting in a uniform radius cylinder. In the latter case, a_1 increases with time and after a certain time, the continuous phase breaks up, forming spherical particles. In order to verify the route of the steepest gradient, phase field simulations are performed with these two initial setups. The coefficients a_1 and a_2 at different times in the simulations are obtained by applying the Fourier transformation to the surface of the continuous phase. The simulation results are represented by the black circles. From the comparison, we see that the GDM paths are well consistent with the simulation results. In Fig. 3(c), the black and green lines (GDM)/circles (simulations) illustrate the evolution paths of two exemplary setups inside the barrier interval, a_1^o/R_0^o 0.48 and 0.55, which transform into a uniform radius cylinder and spherical particles, respectively. For the wavelength $\lambda/(2\pi R_u)$ 0.80 in Fig. 3(c), the critical amplitude for the breakup, which is inside the barrier interval, is found by using binary search algorithm both for GDM and phase field simulations. Repeating this procedure for all other wavelengths, we identify all the critical breakup configurations, as depicted by the red (GDM) and blue (simulation) squares in Fig. 4(a).

4. Geometric criterion

As shown in Fig. 4(a), our simulation results coincide quite well with GDM when $a_1^o/R_0^o \lesssim 0.88$. While $a_1^o/R_0^o > 0.88$, the simulation results become a horizontal line which surprisingly deviates from GDM. A heedful scrutiny on those unusual simulations with large

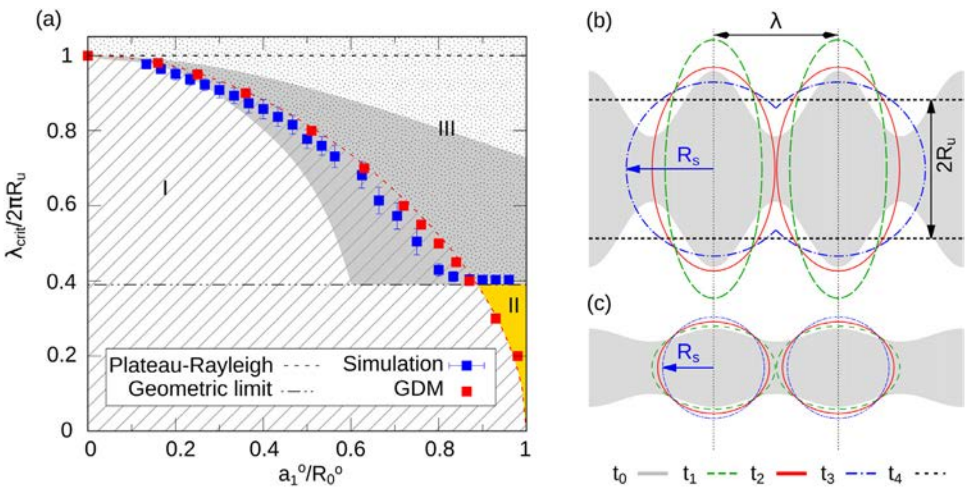

Fig. 4. Stability diagram. (a) The normalized critical breakup wavelength $\lambda_{crit}/(2\pi R_u)$ as a function of the scaled initial amplitude a_1^o/R_0^o. The red and blue squares depict the results from the gradient descent method and the phase-field model, respectively. The red dashed line is the fitting curve for the red squares. The dot-dashed line denotes the geometric criterion. The gray shaded region illustrates all the barrier intervals shown in Fig. 3(c) for different wavelengths. The stability diagram is divided into three regions: I (hatch line), II (orange) and III (excluding I and II, filled with dots). (b) A breakup in II from a continuous phase via separated ellipsoid-shaped particles towards a uniform-radius cylinder. (c) Regular breakup in III, where R_s is the radius of the resulting spheroids.

amplitude perturbations (see Fig. 2(c) iii, a_1^o/R_0^o 0.92) reveals that the continuous phase indeed firstly breaks apart into several oval shaped particles in accordance with GDM. However, afterwards, the spheroidization of the oval particles rebuilds contact between neigh bors and finally leads to a uniform radius cylinder. This process is sketched in Fig. 4(b) and decided by a geometric limit where the dis tance between the centroids of the resulting spheroids $2R_s$ is equal to the wavelength of the perturbation. With the volume conservation condition $\frac{4}{3}\pi R_s^3 \quad \pi R_u^2 \lambda$, the geometric criterion is derived:

$$\lambda_{\text{crit}}^{G} \quad \sqrt{6}R_u,$$

which is shown by the horizontal dot dashed line in Fig. 4(a) and pro vides a reasonable interpretation for those abnormal morphological evolution deviating from GDM in the phase field simulations.

As a result of the geometric constraint, the stability diagram in Fig. 4(a) is divided into three regimes: I (hatch line), II (orange) and III (excluding I and II, filled with dots). In I, the perturbed phase directly evolves into a uniform radius cylinder. In II, the phase firstly trans forms into separated prolate spheroids, elongated in the radial dimension, as shown by the green line in Fig. 4(b). Afterwards, spher oidization rebuilds a chain of connected particles (red and blue lines), which eventually evolves into a uniform radius cylinder (black dashed line). In III, the continuous phase also decomposes into ellip soid shaped particles, which are, however, oblate this time. As sche matically shown in Fig. 4(c), the decrease in the surface area of the oblate spheroids results in an augmentation of the gap spacing between adjacent particles. The demarcation between II and III is defined by the locus that neither prolate nor oblate, but spherical par ticles are precisely tangent to their neighbors. This critical configura tion is actually the geometric limit mentioned above.

5. Comparison with the works in literature

Fig. 5(a) lists several stability criteria from literature. These criteria are graphically depicted in Fig. 5(b). The first one is Plateau Rayleigh's criterion [21 23], which is obtained by comparing the surface area at the perturbed state with the one of a uniform radius cylinder, as shown by Eq. (2). This criterion only considers tiny perturbations and therefore it is only applicable when $a_1^o \ll R_0^o$. With the consideration of finite amplitude perturbations $0 < a_1^o < R_0^o$, Plateau Rayleigh's criterion is extended by Carter and Glaeser [25] & Ma [26]. As can be seen in Fig. 5(b), Carter Glaeser & Ma criterion is well consistent with Plateau Rayleigh's work in the region $a_1^o/R_0^o \ll 1$ and the deviation increases with an increase in the ratio a_1^o/R_0^o. The work of Carter Glaeser & Ma is based on an assumption that at any time the surface of the continuous phase can always be described by a single cosine function (Eq. (6)), so that a_2 is perpetually zero during the evolution. In this case, the path of the surface area minimization is restricted along the line of a_2 0 in Fig. 3(c). The surface area S as a function of a_1 along the line of a_2 0 is shown in Fig. 6, where the red and green circles illustrate two different initial setups a_1^o/R_0^o 0.48 and 0.55, as considered in Fig. 3(c). As we can see in Fig. 6, an energy maximum appears at the right hand side of these two setups and the amplitude a_1 can only decrease with time to reduce the surface area if a_2 is kept at zero. However, when the time evolution of a_2 is taken into account, the amplitude a_1 can increase with time following GDM for the setup a_1^o/R_0^o 0.55 (see the green circles in Fig. 3(c)). This is because that the evolution direction is not solely deter mined by $\partial_{a_1}S$ but is a joint effect of the derivatives $\partial_{a_2}S$ and $\partial_{a_1}S$.

The Nichols Mullins criterion is based on a linear stability analysis on the surface diffusion equation [37,38]

$$\partial_t n \quad d^2\kappa/ds^2,$$

where n is the normal vector of the continuous phase. Assuming tiny perturbations as well as the fact that the surface of the continuous phase can be depicted by a single cosine function, on the one hand, the normal velocity is approximated by the evolution rate of the radius r [37], namely,

$$\partial_t n \approx dr/dt \quad dR_0/dt + (da_1/dt)\cos kz. \tag{14}$$

On the other hand, the mean curvature is approximated as [37] $\kappa \approx 1/r \quad d^2r/dz^2 \quad 1/(R_0 + a_1\cos kz) + a_1k^2\cos kz$. The first and sec ond terms correspond to the radial and longitudinal curvatures, respectively. By using a binomial expansion and only considering the first order terms in a_1, the mean curvature is further rewritten as [37]

$$\kappa \approx 1/R_0 \quad (a_1/R_0^2)\cos kz + a_1k^2\cos kz.$$

With the approximation $d^2\kappa/ds^2 \approx d^2\kappa/dz^2 \quad a_1k^2(1/R_0^2 \quad k^2)\cos kz$, and comparing the coefficient for $\cos kz$ in Eq. (14) with the expression for $d^2\kappa/dz^2$, the evolution equation for the amplitude a_1 is obtained [37]

$$da_1/dt \quad a_1k^2(1/R_0^2 \quad k^2).$$

(a)

Plateau-Rayleigh	Carter-Glaeser & Ma	Nichols-Mullins
$2\pi R_u$	$2\pi R_0^o[1-0.34(a_1^o/R_0^o)^2]$	$2\pi R_0^o$

(b)

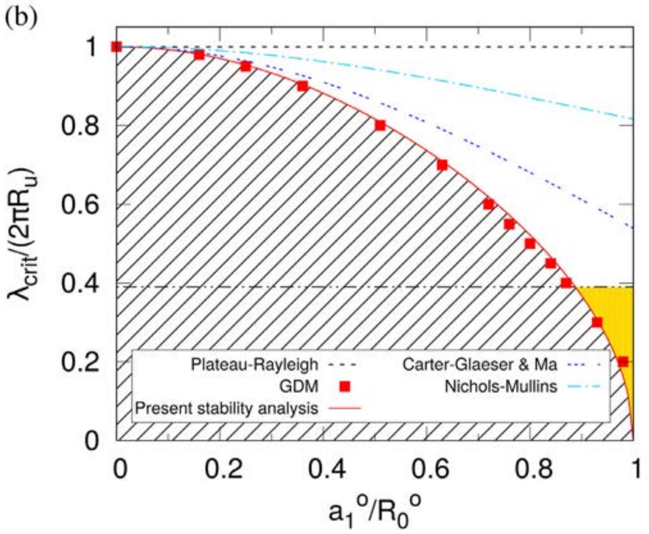

Fig. 5. Comparison with the stability criteria in literature: Plateau-Rayleigh [21,23], Carter-Glaeser [25] & Ma [26], Nichols-Mullins [37].

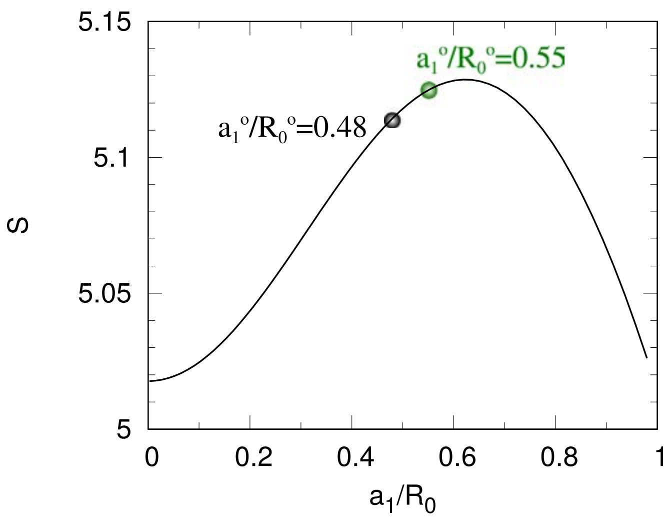

Fig. 6. Surface area as a function of a_1 when a_2 is always zero, corresponding to the horizontal line in Fig. 3(c).

When the amplitude a_1 increases with time, the perturbed phase is morphologically unstable; otherwise, a uniform radius cylinder is the end state. Thus, the condition $da_1/dt \quad 0$ yields the Nichols Mullins criterion [37]

$$\lambda_{crit}^{NM} \quad 2\pi R_0.$$

This criterion can also only be applied for tiny perturbations ($a_1 \ll R_0$) because of the following used approximations: (i) $\partial_t n \approx dr/dt$, (ii) $\kappa \approx 1/r \quad d^2r/dz^2$, (iii) $d^2\kappa/ds^2 \approx d^2\kappa/dz^2$, and (iv) with only first order terms in a_1 for the binomial expansion for the curvature. In order to extend this analysis for a generalized case $0 < a_1^o < R_0^o$, the following changes are made in the present work: (a) $\partial_t n \quad \sqrt{1+(\partial_z r)^2}(dr/dt)$, (b) $\kappa \quad \frac{-\partial_{zz} r}{[1+(\partial_z r)^2]^{3/2}} + \frac{[1+(\partial_z r)^2]}{[1+(\partial_z r)^2]^{3/2}}\frac{1}{r}$, (c) $d^2/ds^2 \quad \frac{1}{\sqrt{1+(\partial_z r)^2}}\frac{d}{dz}\left(\frac{1}{\sqrt{1+(\partial_z r)^2}}\frac{d}{dz}\right)$, (d) with higher order terms in a_1 for the binomial expansion for the curvature. Following the other procedure as the work of Nichols and Mullins, we obtain the following stability criterion (Appendix B)

$$\lambda_{crit} \quad 2\pi\sqrt{R_0^2 \quad a_1^2}. \tag{15}$$

This criterion is illustrated by the red solid line in Fig. 5 and shows quite good agreement with GDM.

By analyzing the surface diffusion equation, the morphological stability has been examined by Ma [40]. The work of Ma is based on a scrutiny on the derivative of the mean curvature $\partial_z\kappa$ in the longitudinal dimension of the perturbed rod. The morphological stability diagram in Ma's work is achieved by a combination of two approaches: (A1) The growth of the perturbation is given by the condition that the least value of the derivative $\partial_z\kappa$ from the crest to the trough is greater than zero. This leads to the regular growth region as highlighted by the dotted region in Fig. 7. (A2) The decay of the perturbation follows the locus that the maximum value of the derivative $\partial_z\kappa$ from the crest to the trough is less than zero. This condition results in the regular decay region as depicted by the hatched region in Fig. 7. (B) The results from (A1) and (A2) are not sufficient to further partition the area between the regular growth and the regular decay regions, since there are scenarios where $\partial_z\kappa$ has negative and positive values from the crest to the trough. In order to define the boundary that distinguishes the growth and the decay regions, Eq. (5) (curve e in Fig. 7), which is derived from the surface area minimization method in a previous work [26], is consulted by Ma. The result from (A1) in combination with Eq. (5) demarcates regular and irregular growth. The result from (A2) in combination with Eq. (5) defines regular and irregular decay.

There are several differences between the present work and the one of Ma [40]. (i) The theory of Ma focuses on analyzing the local value $\partial_z\kappa$ to predict the evolution of the perturbation. When the least value of $\partial_z\kappa$ is greater than zero, the mean curvature monotonically increases from the crest to the trough and the mass is always transported from the trough to the crest. In this case, the rod is morphologically unstable and the corresponding stability criterion is depicted by the curve a in Fig. 7. This result is consistent with our analysis when $\partial_t a_1 > 0$. Contrarily, when the maximum value of $\partial_z\kappa$ is less than zero, the mean curvature monotonically decreases from the crest to the trough and the mass is transferred from the crest to the trough. In this scenario, the rod evolves into a uniform radius cylinder and the corresponding stability criterion is illustrated by the curves b and d in Fig. 7. This result is consistent with our analysis when $\partial_t a_1 < 0$. It is noteworthy that in some cases, there exists both positive and negative values of $\partial_z\kappa$ from the crest to the trough (see Fig. 1(b) in Ref. [26]). These cases correspond to the area between curve a and curves b and d, which cannot be further compartmentalized by the Ma's analysis on the local curvature distribution. Hence, Ma's analysis on $\partial_z\kappa$ falls short to describe the morphological stability for the setups in the region between the curve a and the curves b, d. The present work scrutinizes the evolution of a_1 (Eq. (B.5)) to obtain

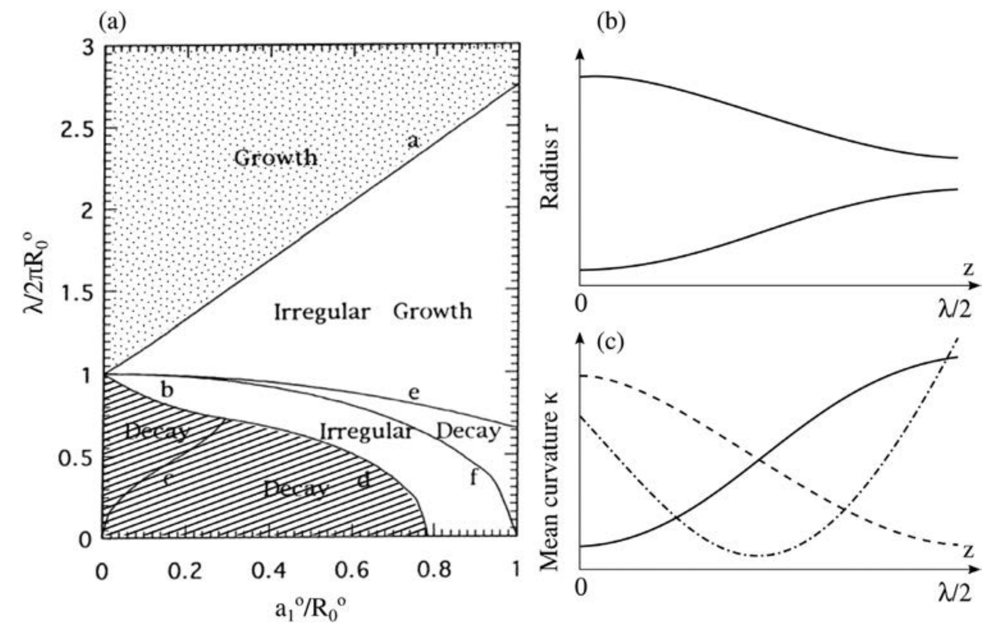

Fig. 7. (a) The critical wavelength as a function of the amplitude from the analysis of Ma [40]. The labels for the *x*- and *y*-axis have been modified to be consistent with the present notations. Here, the dotted and hatched regions are highlighted by the present authors. The region filled with dots (above curve a) is termed as regular growth region, where the mean curvature monotonically increases from the crest to the trough of the perturbation, as sketched by the solid line in (c). The hatched area (below curves b and d) is named as regular decay region, where the mean curvature continuously decreases from the crest to the trough of the perturbation, as schematically shown by the dashed line in (c). When the mean curvature distribution is non-monotonic from the crest to the trough, namely, the existence of a minimum value between the crest and the trough (see Ref. [40] and the dot dashed line in (c)), the perturbation can either grow or decay with time and the corresponding growth/decay behavior is claimed to be irregular by Ma. This irregular growth/decay region is sandwiched between the dot filled area and hatched area. The irregular growth area and irregular decay region are demarcated by the curve e, which is derived from the surface area minimization method in a previous work [26]. The curve f is obtained by the condition that the mean curvatures at the crest and the trough of the perturbation are equal. Reuse with permission, ©1998, Elsevier. (b) Sketch of a continuous phase with a cosinusoidal perturbation. (c) Schematical illustration of the mean curvature distribution for the regular/irregular growth and decay.

the stability criterion, so that an analysis on the local curvature distribution $\partial_z\kappa$ is avoided for the complex cases with non monotonic mean curvature. In order to further partition the area between the curve a and the curves b, d, the surface area minimization method (curve e) from Ref. [40] is adopted by Ma, as discussed in the following. (ii) As an extension of the theory of Ma, an integration from the crest to the through is used for the flux $\partial_z\kappa$ in the longitudinal dimension to calculate the net flux. This integration leads to a comparison between the mean curvatures at the crest and the trough, yielding the same criterion as Eq. (15) (curve f in Fig. 7). As shown in Fig. 5 and Fig. 7, this criterion Eq. (15) is below the one Eq. (5) (curve e). In Ma's work, the area below Eq. (5) is classified as a morphologically stable region and the one between Eq. (5) and Eq. (15) is called as an irregular decay region. It is noteworthy that such a classification is essentially according to Eq. (5) which is derived from the surface area minimization method based on an idealized assumption that the initial single cosinusoidal perturbation always remains harmonic, i.e. $a_n(t) \quad 0, n \in \mathbb{Z}, n \geq 2, \forall t$. As discussed in Fig. 6, this surface area minimization method has actually overestimated the stability criterion because of overlooking higher order amplitudes. As demonstrated in the present work by a more general consideration Eq. (8), the perturbation between Eq. (5) and Eq. (15) (between curves e and f in Fig. 7) can grow with time for the consideration of higher order amplitudes and it is actually a morphologically unstable region.

Another criterion is achieved by comparing the surface area of a uniform radius cylinder $2\pi R_u \lambda$ with the one of a sphere $4\pi R_s^2$, namely, $2\pi R_u \lambda \quad 4\pi R_s^2$. With the volume conservation condition that $\pi R_u^2 \lambda \quad 4\pi R_s^3/3$, we obtain

$$\lambda_{\rm crit}^{CS} \quad 4.5 R_u.$$

As shown in Fig. 3(c) and Fig. 6, an energy barrier may occur in the surface area landscape. Thus, the shortcoming of this stability criterion is that it has overlooked the possible energy barriers between the uniform radius cylinder and the sphere. The criterion of Nayfeh [27]: $\lambda_{\rm crit} \quad 2\pi R_0^o/[1 + 0.75(a_1^o/R_0^o)^2]$, is based on a second order stability analysis on the fluid dynamics equation which is out of the scope of the present discussion.

6. Energetics and kinetics

The work of Nichols Mullins is in the context of kinetics dealing with the surface diffusion equation. In contrast to the kinetic approach, the Plateau Rayleigh criterion Eq. (3) is within the framework of energetics. The Plateau Rayleigh work is derived for an inviscid flow where the surface energy minimization is the only driving force for the morphological evolution, so does the surface diffusion mechanism. In this sense, we believe that the Plateau Rayleigh's criterion should not only be restricted to inviscid flows. In fact, Plateau Rayleigh's criterion has been applied for alloy solidification [1], polymer chains [39], and nanowires [3]. The result of Nichols Mullins is well consistent with the one of Plateau Rayleigh. We are convinced that this consistency is not an accidental event, but due to the fact that the kinetics coincides with the energetics.

The present gradient descent method is from the aspect of energetics by considering the surface area minimization. This concept is similar to that of Plateau Rayleigh which also contemplates the surface area minimization. The current stability analysis is based on the surface diffusion equation by extending the work of Nichols Mullins. The results from these two approaches are nearly the same (see Fig. 5). This is a further evidence for the consistency between energetics and kinetics approaches. Thermodynamically, the morphological evolution of the continuous phase is such as to reduce the surface area because of the non uniform interfacial potential, which is the mean curvature in this case. The surface area minimization can be achieved via different interfacial kinetics, such as surface/bulk diffusion, mean curvature flow, fluid flow or even a mix of them. For instance, Nichols and Mullins [37] show that for different kinetics: surface and bulk diffusion, the stability criteria are identical. It is noted that for surface/bulk diffusion and fluid flow, the volume of the continuous phase is conserved, while for the mean curvature flow, the volume is not preserved. We emphasize that in the present Allen Cahn type method, an additional volume constraint has been provided in order to model a volume conserved mean curvature flow, in contrast to the conventional Allen Cahn model imitating non conserved mean curvature flow. This volume constraint is guaranteed by adding a compensation term $g(\phi)$ in the free energy functional, which has been discussed in Refs. [32,41]. The interfacial kinetics of the volume constraint mean curvature flow may be different from the one of the surface or bulk diffusion (see Ref. [42] for the detailed discussion). Yet, irrespective of the interfacial kinetics, all of them have to follow the thermodynamic concept that the surface area continuously decreases with time. This is probably the underlying reason that the critical breakup condition from the volume constraint Allen Cahn model is nearly the same as the one from the analysis on the surface diffusion equation, at least, the stability criterion from different interfacial kinetics should be inside the gray shaded region in Fig. 4 in order to follow the energetic concept. It has been shown by Garcke [29] that for the interfacial kinetics of surface diffusion, the reduction in the surface area follows the gradient descent path in the H^{-1} space, and that the mean curvature flow obeys the gradient descent route in the L^2 space.

For tiny perturbations $a_1^o/R_0^o \ll 1$, the criteria of Plateau Rayleigh and Nichols Mullins both are independent of the ratio a_1^o/R_0^o, which is in the context of linear stability analysis. By considering large amplitude perturbations, $0 < a_1^o/R_0^o < 1$, the present non linear stability analysis shows that the critical breakup wavelength depends on $(a_1^o/R_0^o)^2$, so do the findings of Carter Glaeser & Ma and Nayfeh. The justifiability of this dependency has been verified by the thermodynamic concept of surface area minimization. The relationship $\lambda \tilde{} (a_1^o/R_0^o)^2$ can also be roughly interpreted as follows. The volume of the perturbed phase is expressed as $V \quad \pi[(R_0^o)^2 + (a_1^o)^2/2]\lambda$, which can be rewritten as $\lambda \quad V/[\pi(R_0^o)^2][(1 + (a_1^o/R_0^o)^2/2]^{-1}$. By using the binomial expansion $[(1 + (a_1^o/R_0^o)^2/2]^{-1} \quad 1 \quad (a_1^o/R_0^o)^2/2 + \mathcal{O}((a_1^o/R_0^o)^4)$, we see that the wavelength is independent of the ratio a_1^o/R_0^o to the first order (linear analysis) and depends on $(a_1^o/R_0^o)^2$ to the next order.

The non uniform mean curvature is the underlying physical reason for the morphological evolution of the perturbed continuous phase. The morphological evolution can be achieved via distinct kinetics: (a) Surface diffusion, (b) bulk diffusion, where the steady state diffusion equation in the bulk has to be subjected to the non uniform Gibbs Thomson potential at the surface, and (c) fluid flow. In the latter kinetics, the non uniform curvature gives rise to a non uniform Laplace pressure along the surface of the perturbed phase, according to the Young Laplace law. The inhomogeneous pressure consequently induces a fluid flow. An additional kinetics is the volume conserved mean curvature flow. Some physical interpretations of the volume conserved mean curvature flow, which corresponds to the phase field approach and the surface area landscape method in the present work, have been narrated in literature [43 45]. For instance, Rubinstein and Sternberg [44] demonstrated that the volume conserved mean curvature flow models a binary mixture undergoing phase separation. The relation of the volume conserved mean curvature flow to the Cahn Hilliard theory and nucleation is also discussed in Ref. [44]. Bronsard and Stoth [45] showed that the phase field model with a volume constraint, which is a kind of non local Ginzburg Landau equation, is a special degenerate limit of a viscous Cahn Hilliard model. As claimed in Ref. [43], the motion of interface driven by the volume conserved mean curvature flow is closely related to the general phenomena of Ostwald ripening. In mathematics, the volume conserved mean curvature flow has been widely studied [41,46]

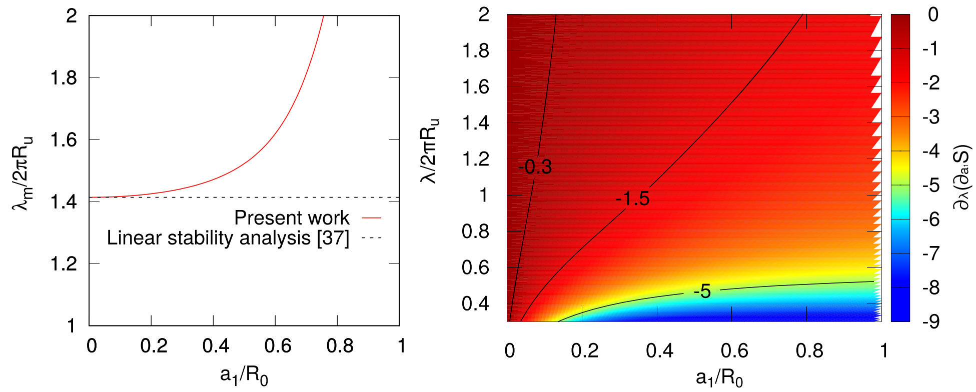

Fig. 8. Different kinetics: (a) The dominant evolution wavelength $\lambda_m/(2\pi R_u)$ as a function of the amplitude a_1/R_0. The red line corresponds to the present work for the surface diffusion mechanism. (b) The derivative $\partial_\lambda(\partial_{a_1}S)$ as a function of a_1/R_0 and $\lambda/(2\pi R_u)$ for a constant volume V 1, corresponding to the surface area landscape method. The numbers on the broken lines depict the corresponding contour levels. The absolute values for the contour levels have to be rescaled with varying the volume.

and considered to be the simplest model problem with nontrivial limiting behavior.

The present finding shows that the critical breakup state for the surface diffusion is the same as the one for the surface energy land scape method as well as for the phase field simulation. The similar finding for the invariance of the critical breakup state has also been found by Nichols and Mullins [37] for surface diffusion and volume diffusion. This invariance has been observed in Ref. [38] for surface diffusion and vapor transport as well. The uniqueness of the critical breakup state is intrinsically decided by thermodynamics. However, the kinetics of different active transport mechanisms may be differ ent. As an example, we estimate the fastest evolution mode in the morphologically unstable region to characterize the kinetic mecha nism. For the surface diffusion mechanism, the fastest growing mode is obtained by finding the zeros after differentiating the right hand side of Eq. (B.5) with respect to the wavelength (see the similar approach in Ref. [37]). The fastest growing wavelength $\lambda_m/(2\pi R_u)$ as a function of the amplitude a_1/R_0 is shown by the red line in Fig. 8(a). For tiny amplitude perturbations $a_1/R_0 \ll 1$, the dominant growth wavelength is consistent with previous linear stability analysis $\lambda_m/(2\pi R_u)$ $\sqrt{2}$ (the horizontal dashed line). For the surface area land scape method, the evolution of the first amplitude a_1 is proportional to the derivative $\partial_{a_1}S$, namely, $\partial_t a_1 \propto \partial_{a_1}S$. Hence, the fastest growing mode is given by the condition that $\varsigma :$ $\partial_\lambda(\partial_{a_1}S)$ 0. Fig. 8(b) depicts the contour plot of ς as a function of $\lambda/(2\pi R_u)$ and a_1/R_0. As can be seen from the contour plot, the value of ς is always negative and the absolute value of ς decreases and approaches zero with an increase in the wavelength. This indicates that there is no maximum growing mode for the surface area landscape method, similar to the vapor transport mechanism (see Ref. [38], noteworthily, this does not mean that the surface area landscape method or phase field model repli cates vapor transport mechanism; exemplary physical scenarios for the surface area landscape method or phase field model are afore discussed). Hence, the comparative studies in Fig. 8 demonstrate, that for different active transport mechanisms, although the critical setup is the same, the kinetics is significantly different. Similar phe nomena of various kinetic mechanisms have been observed for sur face and volume diffusion [37]. It is noteworthy that the derivation of the geometric constraint is based on pure mathematics with a vol ume constraint condition. This derivation is independent of any par ticular kinetic equations. Therefore, the intersection between the geometric limit and the stability criterion in Fig. 4(a) is not affected by the kinetics. It should be emphasized that only when the setup is in the region II and the volume of the phase is conserved, the geomet ric criterion is applicable. In this case, according to thermodynamic contemplation, the perturbed phase has to firstly break up into sepa rate particles in order to reduce the surface energy. The consequent spheroidization of these particles leads to a re establishment of a uni form radius cylinder, arising from the geometric constraint. For a setup outside the region II or not within the plane in Fig. 4 or with a non conserved volume, whether this setup evolves into the region II or not and the effectiveness of the geometric limit remain an open question and shall be discussed regarding the particular kinetics, which is out of the scope of this work.

7. Conclusion and remarks

In summary, we have proposed a generalized model to address the classic Plateau Rayleigh question. As shown in Fig. 5, all the crite ria in literature are above the geometric criterion. Thus, these criteria are not able to elucidate the unusual breakup phenomenon displayed in Fig. 2(c), iii, where the perturbed phase initially breaks up and then again transforms into a uniform radius cylinder. The present cri terion is based on three different methods: (i) surface area calculation plus gradient descent approach, (ii) phase field simulations, (iii) an improved stability analysis. Our criterion crosses with the geometric limit at $a_1^o/R_0^o \approx 0.88$, so that for $a_1^o/R_0^o \lesssim 0.88$, the rod shaped phase directly transforms into a uniform radius cylinder or spherical par ticles. However, for $a_1^o/R_0^o \gtrsim 0.88$, the formation of a uniform radius cylinder undergoes a transient state with dispersed particles. This occurrence of this transient state is solely determined by the wave length λ $\sqrt{6}R_u$, independent of the ratio a_1^o/R_0^o.

Declaration of Competing Interests

The authors declare that they have no known competing financial interests or personal relationships that could have appeared to influ ence the work reported in this paper.

Acknowledgments

The authors thank for support through the coordinated program Virtual Materials Design (VirtMat) within the Helmholtz association and through the Gottfried Wilhelm Leibniz programme NE 822/31. F. W. is grateful to the discussion with W. C. Carter (MIT). F.W. designed the phase field simulations. F.W. and O.T. contributed to the concept of the surface area landscape. F.W., O.T., and H.Z. wrote the first draft of the manuscript. F.W. and H.Z. discussed the gradient descent method. T.L. contributed to the picture illustrating the breakup of a liquid jet under water tap. T.L., B.N., M.S., G.C.M., and J.A. interpreted the thermodynamic concept and revised the manuscript. All authors contributed to the manuscript preparation.

Appendix A. Comparison of the time evolution of the perturbed phase from the phase-field model and the gradient descent method

Fig. A.9 (a) and (b) depict the time evolution of the perturbed phase with $a_1^o/R_0^o \;\; 0.7$, corresponding to the initial setups in Fig. 2(b)iii and Fig. 2(b)ii, respectively. The triangle, circle and square symbols illustrate the simulation results of the phase field model. The red, blue, and green lines are the results from the gradient descent method. The good agreement for the time evolution shows that these two approaches, phase field model and gradient descent method, are consistent with each other.

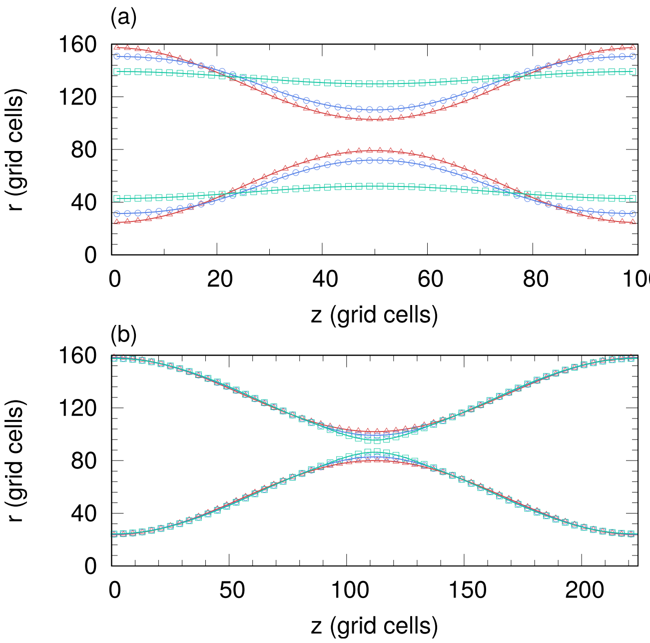

Fig. A9. Time evolution of the perturbed phase for perturbations $a_1^o/R_0^o \;\; 0.7$ with $\lambda/(2\pi R_u) \;\; 0.37$ (a) and 0.8 (b), respectively. In the former case, the continuous phase evolves into a uniform-radius cylinder. In the latter case, the amplitude of the perturbation increases with time and the continuous phase is morphologically unstable. The red, blue, and green colors indicate three times t_0, t_1, and t_2, respectively. The symbols show the phase-field simulation results and the lines illustrate the one of gradient descent method.

Appendix B. A nonlinear stability analysis

After the perturbation, the mean curvature along the surface of the continuous phase is non uniform, which induces a surface flow/diffusion. According to Mullins's theory [37] as well as the textbook work of Balluffi et al. [38], the normal evolution velocity $\partial_t n$ is expressed as $\partial_t n \;\; B\nabla_s^2\kappa$, where κ is the mean curvature. The constant mobility B is defined as $B \;\; \Omega\sigma D^s\delta^*/k_bT$, where Ω is the atomic volume, D^s is the surface diffusivity, δ^* is the thickness of surface and k_b is the Boltzmann constant. On the one hand, by using the euclidean angle $\cos\theta \;\; 1/\sqrt{1+(\partial_z r)^2}$ between the normal and radial directions, the normal velocity is related to the radial evolution rate as $\partial_t n \;\; \sqrt{1+(\partial_z r)^2}(dr/dt)$. On the other hand, by using the relationship, $ds^2 \;\; dr^2+dz^2$, the surface Laplace operator is expressed as [38] $\nabla_s^2 \;\; \frac{1}{\sqrt{1+(\partial_z r)^2}}\frac{d}{dz}\left(\frac{1}{\sqrt{1+(\partial_z r)^2}}\frac{d}{dz}\right)$. With the relationship between the normal velocity and the radial evolution rate as well as the expression for the surface Laplacian, the dynamic equation $\partial_t n \;\; B\nabla_s^2\kappa$ is rewritten as

$$\partial_t R_0 + \partial_t a_1 \cos kz + \cdots \quad \frac{\mathrm{B}}{1+(\partial_z \mathrm{r})^2}\frac{\mathrm{d}}{\mathrm{dz}}\left(\frac{1}{\sqrt{1+(\partial_z \mathrm{r})^2}}\frac{\mathrm{d}\kappa}{\mathrm{dz}}\right). \tag{B.1}$$

The next step is to expand the right hand side of Eq. (B.1) into such a form $c_0 + c_1\cos kz + \cdots$. The dynamic equation for the leading amplitude is expressed as $\partial_t a_1 \;\; c_1$ by comparing the coefficients of the term $\cos kz$ on both sides of Eq. (B.1). The following strategy has been used for the expansion of the right hand side of Eq. (B.1). With the definition $\kappa : \;\; \nabla_s\cdot\mathbf{n}$, where $\mathbf{n}$ is the normal vector of the surface, the mean curvature is expressed as

$$\kappa \quad \frac{\partial_{zz}r}{[1+(\partial_z r)^2]^{3/2}} + \frac{[1+(\partial_z r)^2]}{[1+(\partial_z r)^2]^{3/2}}\frac{1}{r}, \tag{B.2}$$

where the first term is the longitudinal curvature and the second one is the radial curvature. These two curvatures are approximated by the binomial series, namely, $(1+x)^\alpha \;\; 1+\alpha x+\mathcal{O}(x^2)$, as

$$\frac{\partial_{zz}r}{[1+(\partial_z r)^2]^{3/2}} \quad \partial_{zz}r\left[1 \;\; \frac{3}{2}(\partial_z r)^2 + \mathcal{O}((\partial_z r)^4)\right], \tag{B.3}$$

$$\frac{[1+(\partial_z r)^2]}{[1+(\partial_z r)^2]^{3/2}}\frac{1}{r} \quad \frac{1}{R_0}[1+(\partial_z r)^2]\left[1 \;\; \frac{3}{2}(\partial_z r)^2 + \mathcal{O}((\partial_z r)^4)\right][1 \;\; \beta + \mathcal{O}(\beta^2)], \tag{B.4}$$

where $\beta \;\; (a_1\cos kz + a_2\cos 2kz)/R_0$. Here, the following expansions have been used: $[1+(\partial_z r)^2]^{-3/2} \;\; 1 \;\; \frac{3}{2}(\partial_z r)^2 + \mathcal{O}((\partial_z r)^4)$ and $r^{-1} \;\; [1 \;\; \beta + \mathcal{O}(\beta^2)]/R_0$. Substituting Eqs. (B.3) and (B.4) into Eq. (B.2) and making the derivatives according to the right hand side of Eq. (B.1), we obtain the expression for c_1 and the dynamic equation for the leading amplitude

$$\partial_t a_1 \quad B\left[1 \;\; \frac{3}{4}\sum_{n\;\;1}^{\infty}(na_nk)^2\right]^2\left\{k^2 \;\; \frac{1}{R_0^2}\left[1+\sum_{n\;\;1}^{\infty}(na_nk)^2\right]\right\}a_1k^2. \tag{B.5}$$

By evaluating $\partial_t a_1 \;\; 0$, the stability criterion Eq. (15) is obtained.

References

[1] L. Ratke, A. Muller, On the destabilisation of fibrous growth in monotectic alloys, Scr. Mater. 54 (2006) 1217–1220.
[2] A. Kamio, S. Kumai, H. Tezuka, Solidification structure of monotectic alloys, Mater. Sci. Eng. A 146 (1991) 105–121.
[3] H. Oh, J. Lee, M. Lee, Transformation of silver nanowires into nanoparticles by Rayleigh instability: Comparison between laser irradiation and heat treatment, Appl. Surf. Sci. 427 (2018) 65–73.
[4] J.J. Kaufman, et al., Structured spheres generated by an in-fibre fluid instability, Nature 487 (2012) 463.
[5] T. Chakrabarti, N. Verma, S. Manna, Grain boundary driven Plateau–Rayleigh instability in multilayer nanocrystalline thin film: A phase-field study, Mater. Des. 119 (2017) 425–436.
[6] M.K. Santala, A.M. Glaeser, Rayleigh instabilities in crystalline solids: Evolution of finite-aspect-ratio pore channels in sapphire, Acta Mater. 56 (2008) 1967–1980.
[7] G.H. Kim, C.V. Thompson, Effect of surface energy anisotropy on Rayleigh-like solid-state dewetting and nanowire stability, Acta Mater. 84 (2015) 190–201.
[8] J.R. Royer, et al., High-speed tracking of rupture and clustering in freely falling granular streams, Nature 459 (2009) 1110.
[9] M. Moseler, U. Landman, Formation, stability, and breakup of nanojets, Science 289 (2000) 1165.
[10] A.S. Utada, E.L. Lorenceau, D.R. Link, P. D. Kaplan, H.A. Stone, D.A. Weitz, Monodisperse double emulsions generated from a microcapillary device, Science 308 (2005) 537.
[11] S. Haefner, et al., Influence of slip on the Plateau–Rayleigh instability on a fibre, Nat. Commun. 6 (2015) 7409.
[12] V. Cardoso, O.J.C. Dias, Rayleigh-Plateau and Gregory-Laflamme instabilities of black strings, Phys. Rev. Lett. 96 (2006) 181601.
[13] G. Prado, Y. Amarouchene, H. Kellay, Experimental evidence of a Rayleigh-Plateau instability in free falling granular jets, Phys. Rev. Lett. 106 (2011) 198001.
[14] F. Wang, B. Nestler, Detachment of nanowires driven by capillarity, Scr. Mater. 113 (2016) 167–170.
[15] F. Wang, R. Mukherjee, M. Selzer, B. Nestler, Numerical study on solutal Marangoni instability in finite systems with a miscibility gap, Phys. Fluids 26 (2014) 124102.

[16] H. Wijshoff, The dynamics of the piezo inkjet printhead operation, Phys. Rep. 491 (2010) 77.
[17] P.P. Bhat, et al., Formation of beads-on-a-string structures during break-up of viscoelastic filaments, Nat. Phys. 6 (2010) 625.
[18] Z. Xue, et al., Engineering island-chain silicon nanowires via a droplet mediated Plateau-Rayleigh transformation, Nat. Commun. 7 (2016) 12836.
[19] E.C. Garnett, et al., Self-limited plasmonic welding of silver nanowire junctions, Nat. Mater. 11 (2012) 241.
[20] R.W. Day, et al., Plateau–Rayleigh crystal growth of periodic shells on one-dimensional substrates, Nat. Nanotechnol. 10 (2015) 345.
[21] J. Plateau, Statique expérimentale et théorique des liquides soumis aux seules forces moléculaires, Gauthier-Villars, 1873.
[22] L. Rayleigh, On the instability of jets, Proc. Math. Soc. 10 (1878) 4.
[23] L. Rayleigh, On the capillary phenomena of jets, Proc. Math. Soc. 29 (1879) 196.
[24] T.F. Marinis, R.F. Sekerka, F.D. Lemkey, H.E. Cline, M. Mcclean, Situ Composites IV, Elsevier, NY, 1982, pp. 315–327.
[25] W.C. Carter, A.M. Glaeser, The effect of finite amplitude perturbations on the stability of continuous phases, Mater. Sci. Eng. 89 (1987) 41.
[26] M. Qian, S. Harada, B. Liu, On the critical instability wavelengths of rod morphologies containing an arbitrary sinusoidal perturbation, Mater. Sci. Eng. A 221 (1996) 192–194.
[27] A.H. Nayfeh, Nonlinear stability of a liquid jet, Phys. Fluids 13 (1970) 841.
[28] F. Wang, Effect of Capillarity on the Breakup of Liquid Jets, Interfacial Wave and Motion of Droplets in Immiscible Liquids, Karlsruhe Institute of Technology, 2017 Phd dissertation.
[29] H. Garcke, Curvature driven interface evolution, Jahresbericht der Deutschen Mathematiker-Vereinigung 115 (2013) 63–100.
[30] F. Wang, P. Altschuh, A.M Matz, J. Heimann, B.S. Matz, B. Nestler, N. Jost, Phase-field study on the growth of magnesium silicide occasioned by reactive diffusion on the surface of Si-foams, Acta Mater. 170 (2019) 138–154.
[31] S.M. Allen, J.W. Cahn, A microscopic theory for antiphase boundary motion and its application to antiphase domain coarsening, Acta Metall. 27 (1979) 1085–1095.
[32] B. Nestler, F. Wendler, M. Selzer, B. Stinner, H. Garcke, Phase-field model for multiphase systems with preserved volume fractions, Phys. Rev. E 78 (2008) 011604.
[33] Y. Wu, F. Wang, M. Selzer, B. Nestler, Investigation of equilibrium droplet-shapes on chemically striped patterned surfaces using phase-field method, Langmuir 35 (2019) 8500–8516.
[34] M. Zimmermann, A. Karma, M. Carrard, Oscillatory lamellar microstructure in off-eutectic Al-Cu alloys, Phys. Rev. B 42 (1990) 833.
[35] A. Choudhury, M. Plapp, B. Nestler, Theoretical and numerical study of lamellar eutectic three-phase growth in ternary alloys, Phys. Rev. E 83 (2011) 051608.
[36] B. Nestler, A.A. Wheeler, L. Ratke, L.C. Stocker, Phase-field model for solidification of a monotectic alloy with convection, Physica D 141 (2000) 133–154.
[37] F.A. Nichols, W.W. Mullins, Surface- (interface-) and volume-diffusion contributions to morphological changes driven by capillarity, Trans. Metall. Soc. AIME 233 (1965) 1840–1848.
[38] R.W. Balluffi, S.M. Allen, W.C. Carter, Kinetics of materials, John Wiley & Sons (2005).
[39] B.J. Haupt, T.J. Senden, E.M. Sevick, AFM evidence of Rayleigh instability in single polymer chains, Langmuir 18 (2002) 2174–2182.
[40] Q. Ma, Non-linear capillary shape evolution of rod morphologies via interfacial diffusion, Acta Mater. 46 (1998) 1669–1681.
[41] H. Garcke, B. Nestler, B. Stinner, F. Wendler, Allen–Cahn systems with volume constraints, Math. Models Methods Appl. Sci. 18 (2008) 1347–1381.
[42] D. Lee, J. Kim, Comparison study of the conservative Allen–Cahn and the Cahn–Hilliard equations, Math. Comput. Simul. 119 (2016) 35–56.
[43] S.J. Ruuth, B.T.R. Wetton, A simple scheme for volume-preserving motion by mean curvature, J. Sci. Comput. 19 (2003) 373–384.
[44] J. Rubinstein, P. Sternberg, Nonlocal reaction–diffusion equations and nucleation, IMA J. Appl. Math. 48 (1992) 249–264.
[45] L. Bronsard, B. Stoth, Volume-preserving mean curvature flow as a limit of a nonlocal Ginzburg-Landau equation, SIAM J. Math. Anal. 28 (1997) 769–807.
[46] X. Chen, D. Hilhorst, E. Logak, Mass conserving Allen–Cahn equation and volume preserving mean curvature flow, Interfaces Free Bound. 12 (2011) 527–549.